

Fluctuations of harmonic and radial flow in heavy ion collisions with principal components

Aleksas Mazeliauskas* and Derek Teaney†

Department of Physics and Astronomy, Stony Brook University, Stony Brook, New York 11794, USA

(Dated: October 13, 2018)

We analyze the spectrum of harmonic flow, $v_n(p_T)$ for $n = 0-5$, in event-by-event hydrodynamic simulations of Pb+Pb collisions at the CERN Large Hadron Collider ($\sqrt{s_{NN}} = 2.76$ TeV) with principal component analysis (PCA). The PCA procedure finds two dominant contributions to the two-particle correlation function. The leading component is identified with the event plane $v_n(p_T)$, while the subleading component is responsible for factorization breaking in hydrodynamics. For v_0 , v_1 , and v_3 the subleading flow is a response to the radial excitation of the corresponding eccentricity. By contrast, for v_2 the subleading flow in *peripheral collisions* is dominated by the nonlinear mixing between the leading elliptic flow and radial flow fluctuations. In the v_2 case, the sub-sub-leading mode more closely reflects the response to the radial excitation of ε_2 . A consequence of this picture is that the elliptic flow fluctuations and factorization breaking change rapidly with centrality, and in central collisions (where the leading v_2 is small and nonlinear effects can be neglected) the subsub-leading mode becomes important. Radial flow fluctuations and nonlinear mixing also play a significant role in the factorization breaking of v_4 and v_5 . We construct good geometric predictors for the orientation and magnitudes of the leading and subleading flows based on a linear response to the geometry, and a quadratic mixing between the leading principal components. Finally, we suggest a set of measurements involving three point correlations which can experimentally corroborate the nonlinear mixing of radial and elliptic flow and its important contribution to factorization breaking as a function of centrality.

I. INTRODUCTION

Two-particle correlation measurements are of paramount importance in studying ultrarelativistic heavy ion collisions, and provide an extraordinarily stringent test for theoretical models. Indeed, the measured two-particle correlations exhibit elliptic, triangular, and higher harmonics flows, which can be used to constrain the transport properties of the quark gluon plasma (QGP) [1, 2]. The remarkable precision of the experimental data as a function of transverse momentum and pseudorapidity has led to new analyses of factorization breaking, nonlinear mixing, event shape selection, and forward-backward fluctuations [3–8]. In this paper we analyze the detailed structure of two-particle transverse momentum correlations by using event-by-event (boost-invariant) hydrodynamics and principal component analysis (PCA) [9, 10]. Specifically, we decompose the event-by-event harmonic flow $V_n(p_T)$ into principal components and investigate the physical origin of each of these fluctuations. This paper extends our previous analysis [10] for triangular flow at the LHC (Pb+Pb at $\sqrt{s_{NN}} = 2.76$ TeV) to the other harmonics, $n = 0-5$. In particular, we demonstrate the importance of radial flow fluctuations for subleading flows of higher harmonics.

Taking the second harmonic for definiteness, the two-particle correlation matrix of momentum dependent elliptic flows, $C_2(p_{T1}, p_{T2}) \equiv \langle V_2(p_{T1})V_2^*(p_{T2}) \rangle$ is tradi-

tionally parametrized by $r_2(p_{T1}, p_{T2})$ [11],

$$r_2(p_{T1}, p_{T2}) \equiv \frac{\langle V_2(p_{T1})V_2^*(p_{T2}) \rangle}{\sqrt{\langle |V_2(p_{T1})|^2 \rangle \langle |V_2(p_{T2})|^2 \rangle}}. \quad (1)$$

If there is only one source of elliptic flow in the event [for example if in each event $V_2(p_T) = f(p_T)\varepsilon_2$ with ε_2 a complex eccentricity and $f(p_T)$ a fixed real function of p_T] then the correlation matrix of elliptic flows $C_2(p_{T1}, p_{T2})$ factorizes into a product of functions, and the r_2 parameter is unity. However, if there are multiple independent sources of elliptic flow in the event, then the correlation matrix does not factorize, and the r_2 parameter is less than unity [11]. The r_2 parameter has been extensively studied both experimentally [3, 12–14] and theoretically [10, 11, 15, 16]. In particular, in our prior work on triangular flow we showed that factorization breaking in event-by-event hydrodynamics arises because the simulated triangular flow is predominantly the result of two statistically uncorrelated contributions—the linear response to ε_3 [17] and the linear response to the first radial excitation of ε_3 [10]. The goal of the current paper is to extend this understanding of factorization breaking to the other harmonics. This extension was surprisingly subtle due to the quadratic mixing between the leading and subleading harmonic flows.

Experimentally, it is observed that factorization breaking is largest for elliptic flow in central collisions (see in particular Fig. 28 of Ref. [13] and Fig. 1 of Ref. [3]). Indeed, the r_2 parameter decreases rather dramatically from mid-central to central collisions. This indicates that the relative importance of the various initial state fluctuations which drive elliptic flow are changing rapidly as a function of centrality. The current manuscript explains

* aleksas.mazeliauskas@stonybrook.edu

† derek.teaney@stonybrook.edu

the rapid centrality dependence of factorization breaking in v_2 as an interplay between the linear response to the fluctuating elliptic geometry, and the nonlinear mixing of the radial flow and average elliptic flow. This quadratic mixing is similar to the mixing between v_5 and v_2, v_3 [18–21], and this picture can be confirmed experimentally by measuring specific three point correlations analogous to the three plane correlations measured in the v_5, v_2, v_3 case [4, 5].

To understand the linear and nonlinear contributions quantitatively, we will break up the fluctuations in hydrodynamics into their principal components, and analyze the linear and nonlinear contributions of each principal component to the simulated harmonic spectrum. The sample of events and most of the PCA methods are the same as in our previous paper [10], and therefore in Sects. II A and II B we only briefly review the analysis definitions, and the key features of simulations. In Sect. II C we discuss the strategy for constructing the best linear predictor for leading and subleading flows.

The second part of our paper, Sect. III, contains individual discussions for each harmonic flow. First, we discuss radial flow fluctuations in Sect. III A and then demonstrate their importance in generating subleading elliptic flow in Sect. III B 1. In Sect. III C we briefly describe our PCA results for direct and triangular flows. Finally, in Sect. III D we discuss the quadrangular and pentagonal flows and how the nonlinear mixing of lower order principal components adds to these flows. We put forward some experimental observables in the discussion in Sect. IV. A catalog of figures showing the main results of PCA for each harmonic is given in the Appendix.

II. PCA OF TWO-PARTICLE CORRELATIONS IN EVENT-BY-EVENT HYDRODYNAMICS

A. Principal components

PCA is a statistical technique for extracting the dominant components in fluctuating data. In the context of flow in heavy ion collisions it was first introduced in Ref. [9], and then applied to the analysis of triangular flow in our previous paper [10]. Here we review the essential definitions.

The event-by-event single particle distribution is customarily expanded in a Fourier series

$$\frac{dN}{d\mathbf{p}} = V_0(p_T) + \sum_{n=1}^{\infty} V_n(p_T) e^{-in\varphi} + \text{H.c.}, \quad (2)$$

where $d\mathbf{p} = dy dp_T d\varphi$ denotes the phase space, φ is the azimuthal angle of the distribution, and H.c. denotes Hermitian conjugate. $V_n(p_T)$ is a complex Fourier coefficient recording the magnitude and orientation of the n th harmonic flow, without the typical normalization by multiplicity.

PCA is done by expanding the covariance matrix of two-particle correlations (which is real, symmetric, and

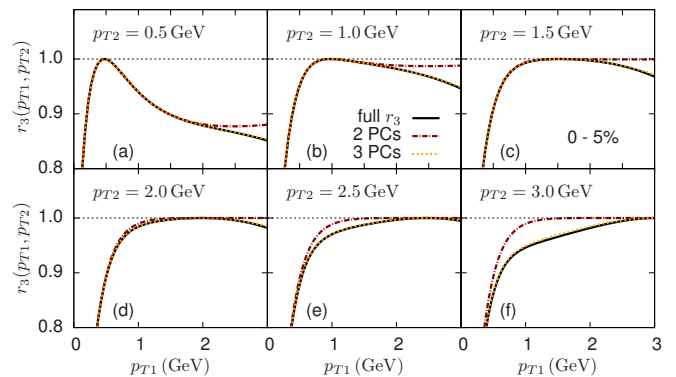


FIG. 1. Factorization ratio $r_3(p_{T1}, p_{T2})$ [Eq. (7)] for triangular flow and its approximations with principal components (PCs) in central collisions (0–5%).

positive semi-definite) into real orthogonal eigenvectors $V_n^{(a)}(p_T)$,

$$C_n(p_{T1}, p_{T2}) \equiv \langle (V_{n,p_{T1}} - \langle V_{n,p_{T1}} \rangle) (V_{n,p_{T2}}^* - \langle V_{n,p_{T2}}^* \rangle) \rangle \\ = \sum_a V_n^{(a)}(p_{T1}) V_n^{(a)}(p_{T2}), \quad (3)$$

where $V_n^{(a)} = \sqrt{\lambda_a} \psi^{(a)}(p_T)$ is the square root of the eigenvalue times a normalized eigenvector. The eigenvalue records the squared variance of a given fluctuation.

The principal components $V_n^{(1)}(p_T), V_n^{(2)}(p_T), \dots$ of a given event ensemble can be used as optimal basis for event-by-event expansion of harmonic flow

$$V_n(p_T) - \langle V_n(p_T) \rangle = \xi_n^{(1)} V_n^{(1)}(p_T) + \xi_n^{(2)} V_n^{(2)}(p_T) + \dots \quad (4)$$

The complex coefficients $\xi_n^{(a)}$ are the projections of harmonic flow onto principal component basis and record the orientation and event-by-event amplitude of their respective flows. Principal components are mutually uncorrelated

$$\langle \xi_n^{(a)} \xi_n^{*(b)} \rangle = \delta^{ab}. \quad (5)$$

Typically the eigenvalues of $C_n(p_{T1}, p_{T2})$ are strongly ordered and only the first few terms in the expansion are significant. Often the large components have a definite physical interpretation. We define the scaled magnitude of the flow vector $V_n^{(a)}(p_T)$ as

$$\|v_n^{(a)}\|^2 \equiv \frac{\int (V_n^{(a)}(p_T))^2 dp_T}{\int \langle dN/dp_T \rangle^2 dp_T}, \quad (6)$$

which is a measure of the size of the fluctuation without trivial dependencies on the mean multiplicity in a given centrality class.

The leading flow vector $V_n^{(1)}(p_T)$ corresponds to fluctuations with the largest root-mean-square amplitude, while subsequent components maximize the variance

in the remaining orthogonal directions. This yields a very efficient description of the full covariance matrix $C_n(p_{T1}, p_{T2})$ and factorization ratio

$$r_n(p_{T1}, p_{T2}) \equiv \frac{C_n(p_{T1}, p_{T2})}{\sqrt{C_n(p_{T1}, p_{T1})C_n(p_{T2}, p_{T2})}} \leq 1. \quad (7)$$

$r_n(p_{T1}, p_{T2})$ is bounded by unity within hydrodynamics [11]. By truncating series expansion of the covariance matrix [Eq. (3)] at two or three principal components we can approximate $C_n(p_{T1}, p_{T2})$ and $r_n(p_{T1}, p_{T2})$. Truncating at the leading term would constitute complete flow factorization, i.e., $r_n = 1$. The factorization matrix for triangular flow is shown in Fig. 1. We see that at low momentum $p_T < 2$ GeV just two principal components are sufficient to describe momentum dependence of factorization ratio r_3 . Analogous decompositions of two-particle correlations into principal components exist for all harmonics and all centralities. Interpreting these large flow components physically is the goal of this paper.

B. Simulations

We used boost-invariant event-by-event viscous hydrodynamics to simulate 5000 Pb-Pb collisions at the CERN Large Hadron Collider (LHC) ($\sqrt{s_{NN}} = 2.76$ TeV) in fourteen 5% centrality classes selected by impact parameter. The initial conditions are based on the Phobos Glauber Monte Carlo [17] with a two-component model for the entropy distribution in the transverse plane. We used a lattice equation of state [22] and a “direct” pion freeze-out at $T_{fo} = 140$ MeV. The results presented here were simulated using a shear viscosity to entropy ratio of $\eta/s = 0.08$. Qualitatively similar results are obtained with $\eta/s = 0.16$, with the most important differences discussed in Sect. III B 2. The same ensemble of events was used in Ref. [10], which provides further simulation details.

C. Geometrical predictors

We will construct several geometric predictors for the leading and subleading flows following strategy outlined in Ref. [20]. Keeping the discussion general, let $\xi_n^{(a)}$ be a geometric quantity which predicts the event-by-event amplitude and phase of the corresponding flow $\xi_n^{(a)}$. For example, for the leading $n = 3$ component the triangularity $\varepsilon_{3,3}$ (defined below) is an excellent choice for $\xi_{3, \text{pred}}^{(1)}$.

The geometric predictors are designed to maximize the correlation between a particular flow signal and the geometry. Specifically, the predictors maximize the Pearson correlation coefficient between the event-by-event magnitude and orientation of a th principal component,

$\xi_n^{(a)}$, and the geometrical predictor $\xi_n^{(a)}$ pred

$$\max Q_n^{(a)} = \frac{\langle \xi_n^{(a)} \xi_n^{*(a)} \rangle}{\sqrt{\langle \xi_n^{(a)} \xi_n^{*(a)} \rangle \langle \xi_n^{(a)} \xi_n^{*(a)} \rangle}}. \quad (8)$$

We constructed several predictors for the flow $\xi_n^{(a)}$ by assuming a linear relation between the flow and the geometry. The simplest predictor consists of linear combinations of the first two eccentricities of the initial geometry. These are defined as

$$\varepsilon_{n,n} \equiv -\frac{[r^n e^{in\phi}]}{R_{\text{rms}}^n}, \quad (9a)$$

$$\varepsilon_{n,n+2} \equiv -\frac{[r^{n+2} e^{in\phi}]}{R_{\text{rms}}^{n+2}}, \quad (9b)$$

where the square brackets $[\]$ denote an integral over the initial entropy density for a specific event, normalized by the average total entropy \bar{S}_{tot} . $R_{\text{rms}} \equiv \sqrt{\langle [r^2] \rangle}$ is the event averaged root-mean-square radius. Note that our definitions of $\varepsilon_{n,n}$ and $\varepsilon_{n,n+2}$ are chosen to make the event-by-event quantities $\varepsilon_{n,n}$ and $\varepsilon_{n,n+2}$ linear in the fluctuations. In this notation, the geometric predictor based on these eccentricities is

$$\xi_n^{(a)} \text{ pred} = \varepsilon_{n,n} + c_1 \varepsilon_{n,n+2}, \quad (10)$$

where c_1 is adjusted to maximize the correlation coefficient in Eq. (8), and the overall normalization is irrelevant. While the first two eccentricities provide an excellent predictor for the leading flow, they do not predict the subleading flow very well. This is in part because the radial weight r^{n+2} is too strong at large r .

More generally, one can define eccentricity as a functional of radial weight function $\rho(r)$:

$$\varepsilon_n \{ \rho(r) \} \equiv -\frac{[\rho(r) e^{in\phi}]}{R_{\text{rms}}^n}. \quad (11)$$

It is the goal of this paper to find the optimal radial weight function $\rho(r)$ for predicting both leading and subleading flows. For the subleading modes $\rho(r)$ will have a node, and thus $\varepsilon_n \{ \rho(r) \}$ will measure the magnitude and orientation of the first radial excitation of the geometry [10].

To find the optimal radial weight we expand $\rho(r)$ in radial Fourier modes

$$\rho(r) = \sum_{b=1}^{n_k} w_b \frac{2^n n!}{k_b^n} J_n(k_b r), \quad (12)$$

where $J_n(x)$ is a Bessel function of order n , w_b are expansion coefficients, and k_b are definite wavenumbers specified below. The prefactor is chosen so that for a single k mode ($w_1 = 1, w_{b>1} = 0$) at small k ($k R_{\text{rms}} \ll 1$) the generalized eccentricity approaches $\varepsilon_{n,n}$

$$\lim_{k \rightarrow 0} \varepsilon_n \{ \rho(r) \} = \varepsilon_{n,n}. \quad (13)$$

At small k , we expand the $J_n(kr)$ and find

$$\varepsilon_n\{\rho(r)\} \simeq \varepsilon_{n,n} + c_1 \varepsilon_{n,n+2}, \quad (14)$$

where $c_1 = -(kR_{\text{rms}}/2)^2/(1+n)$. Thus the functional form of $\rho(r)$ adopted here yields a tunable linear combination of the eccentricities in Eq. (9), but the wave number parameter regulates the behavior at large r . Further motivation and discussion of this basis set for $\rho(r)$ is given in our previous work [10].

We have found that an approximately optimal radial weight can be found by using only two well chosen k_b values for the Fourier expansion in Eq. (12). Including additional k modes in the functional form of $\rho(r)$ does not significantly improve the predictive power of the generalized geometric eccentricity. For the two k modes we required (somewhat arbitrarily) that the ratio of k values would be fixed to the ratio of the first two Bessel zeros:

$$\frac{k_1}{k_2} = \frac{j_{n,1}}{j_{n,2}}. \quad (15)$$

With this choice our basis functions were orthogonal in the interval $[0, R_o]$, where $k_1 = j_{n,1}/R_o$. We then adjusted R_o to maximize the correlation coefficient between $\varepsilon_n\{\rho(r)\}$ and the flow $\xi_n^{(a)}$. To account for changing system size with centrality, we used a fixed R_o/R_{rms} ratio. In most cases we used $R_o/R_{\text{rms}} \approx 3.0$, but for all directed flow components ($\xi_1^{(1)}$ and $\xi_1^{(2)}$) and the second elliptic flow component ($\xi_2^{(2)}$), we found that $R_o/R_{\text{rms}} \approx 2.0$ optimized the correlation between the flow and the geometry.

Ultimately, the assumption that the amplitude and phase of the flow is determined at least approximately by initial eccentricity, $\varepsilon_n\{\rho(r)\}$, is based on linear response. If nonlinear physics becomes important (as in the case of v_4 and v_5) then the predictors should be modified to incorporate this physics (see below and Ref. [20]). Thus, below we will refer to the $\varepsilon_n\{\rho(r)\}$ (with an optimized radial weight) as the *best linear predictor* and incorporate quadratic nonlinear corrections to the predictor as needed.

III. RESULTS

A. Radial flow

Radial flow (or $V_0(p_T)$) is the first term in the Fourier series and is by far the largest harmonic. Traditionally, the experimental and theoretical study of the fluctuations of $V_0(p_T)$ (i.e., multiplicity and p_T fluctuations) has been distinct from elliptic and triangular flow. There is no reason for this distinction.

Examining the scaled $V_0(p_T)$ eigenvalues shown in Fig. 2(a), we see that there are two large principal components. The first principal component is sourced by multiplicity fluctuations, i.e., the magnitude of $V_0(p_T)$

fluctuates (but not its shape) due to the impact parameter variance in a given centrality bin. Corroborating this inference, Fig. 2(a) shows the momentum dependence of the leading principal component, which is approximately flat.¹ Clearly this principal component is not particularly interesting, and the PCA procedure gives a practical method for isolating these trivial geometric fluctuations in the data set. The second principal component is of much greater interest, and shows a linear rise with p_T that is indicative of the fluctuations in the radial flow velocity of the fluid [9].

In early insightful papers [23, 24], the fluctuations in the flow velocity (or mean p_T) were associated with the fluctuations in the initial fireball radius. These radial fluctuations are well described by both the eccentricities ($\varepsilon_{0,0}$, $\varepsilon_{0,2}$), Eq. (9), and the optimized eccentricity $\varepsilon_0\{\rho(r)\}$, Eq. (11). Therefore, as seen in Fig. 2(b), the subleading flow signal is strongly correlated with these linear geometric predictors.

Also shown in Fig. 2(b) is the correlation between subleading radial flow $\xi_0^{(2)}$ and mean transverse momentum fluctuations around the average

$$\delta p_T \equiv [p_T] - \langle [p_T] \rangle. \quad (16)$$

Indeed, the subleading radial flow correlates very well with mean momentum fluctuations in all centrality bins.

In the next sections we will study the nonlinear mixing between the radial flow $\xi_0^{(2)}$ and all other harmonics.

B. Elliptic flow

1. Nonlinear mixing and elliptic flow

We next study the fluctuations of $V_2(p_T)$ as function of centrality. As seen in Fig. 3, the principal component spectrum of elliptic flow in central collisions consists of two nearly degenerate subleading components in addition to the dominant leading component. This degeneracy is lifted in more peripheral bins. Comparing the p_T dependence of the principal flows shown in Figs. 4(a) and 4(b), we see that going from central (0–5%) to peripheral (45–50%) collisions, the magnitude of the second principal component increases in size and its momentum dependence changes dramatically. By contrast, the growth of the third principal component is much more mild. This strongly suggests that the average elliptic geometry is more important for the subleading than the subsub-leading mode.

¹ There is a small upward tending slope in our simulations of this component, because multiplicity and mean p_T fluctuations only approximately factorize into leading and subleading principal components. Using different definitions of centrality bins could perhaps make this separation cleaner.

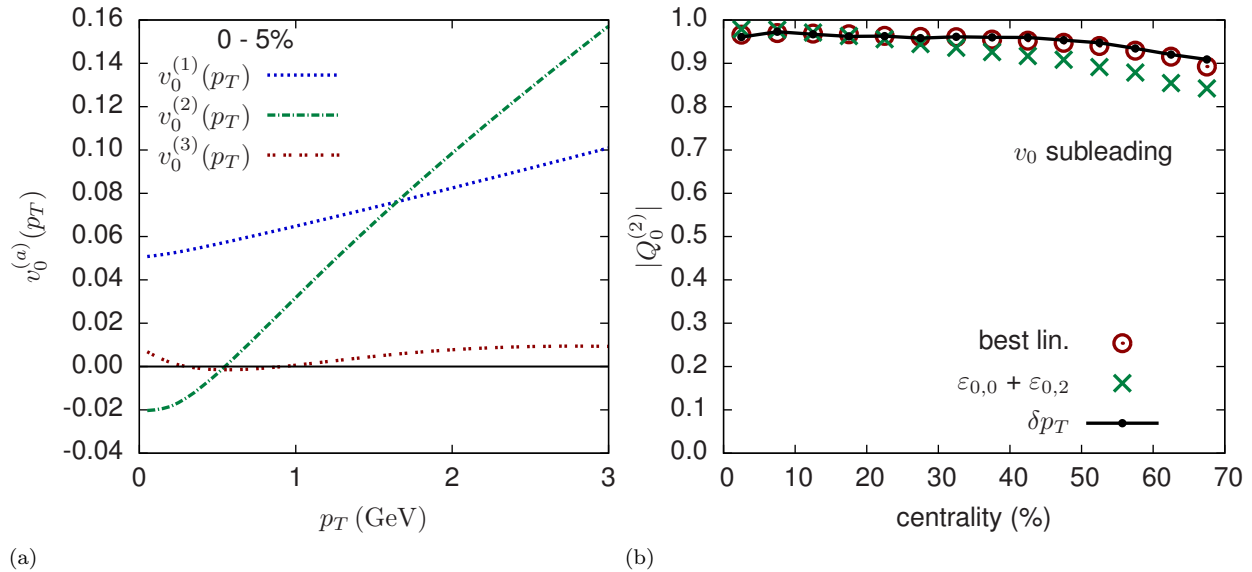


FIG. 2. (a) The p_T dependence of the principal components of radial flow normalized by the average multiplicity, $v_0^{(a)}(p_T) \equiv V_0^{(a)}(p_T) / \langle dN/dp_T \rangle$. (b) The Pearson correlation coefficient [Eq. (8)] between the subleading radial flow and various predictors versus centrality. The best linear predictor is described in Sect. II C.

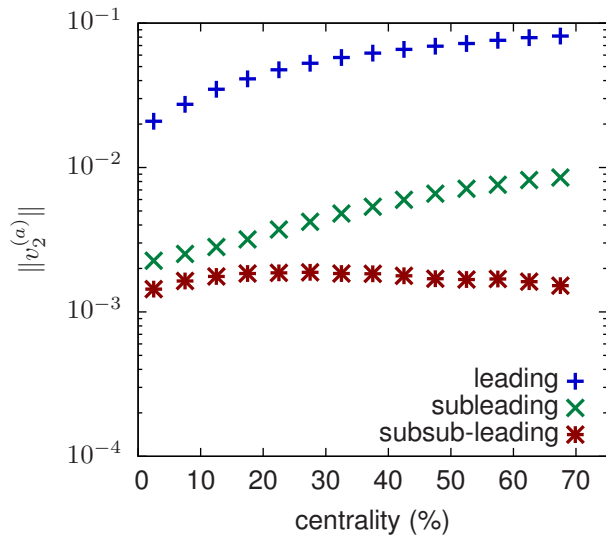


FIG. 3. The magnitudes of the principal components of elliptic flow, $\|v_2^{(a)}\|$, versus centrality [see Eq. (6)].

To find a geometrical predictor for the sub- and sub-sub-leading modes we first tried the best linear predictor $\varepsilon_2\{\rho(r)\}$. In Fig. 5(a) (the red circles), we see that the correlation coefficient between this optimal linear predictor and the subleading flow signal drops precipitously as a function of centrality. As we will explain now, this is because nonlinear mixing becomes important for the subleading mode.

The ellipticity of the almond shaped geometry in peripheral collisions is traditionally parametrized by eccentricity $\varepsilon_{2,2}$ and it serves as an excellent predictor for

the leading elliptic flow. However, $\varepsilon_{2,2}$ does not completely fix the initial geometry, and the radial size of the fireball can fluctuate at fixed eccentricity. As explained in Sect. III A, the radial size fluctuations modulate the momentum spectrum of the produced particles, and for a background geometry with large *constant* eccentricity this generates fluctuations in the p_T dependence of the elliptic flow, i.e., subleading elliptic flow. This subleading flow lies in the reaction plane following the average elliptic flow, but its sign (which is determined by δp_T) is uncorrelated with $\varepsilon_{2,2}$.

The orientation of the reaction plane in peripheral bins is strongly correlated with the integrated v_2 or the leading elliptic principal component $\xi_2^{(1)}$, while the mean p_T fluctuations are tracked by the subleading radial flow component $\xi_0^{(2)}$. Therefore we correlated the sub- and sub-sub-leading elliptic flows with the product of the leading elliptic and radial flows, i.e. we computed the correlation coefficient in Eq. (8) with $\xi_{2,\text{pred}}^{(2)} = \xi_2^{(1)}\xi_0^{(2)}$. Examining Fig. 5(a) (the black line), we see that the correlation between the subleading elliptic flow and the nonlinear mixing rises with centrality, as the correlation with best linear predictor drops. Examining Fig. 5(b) on the other hand, we see that the subsub-leading elliptic flow has stronger correlation with the initial geometry than the nonlinear mixing. Combining best linear geometric predictor and quadratic mixing terms in the predictor, i.e.

$$\xi_{2,\text{pred}}^{(2)} = \varepsilon_2\{\rho(r)\} + c_1\xi_2^{(1)}\xi_0^{(2)}, \quad (17)$$

we achieve consistently high correlations for all centralities [the blue diamonds in Fig. 5(a) and (b)].

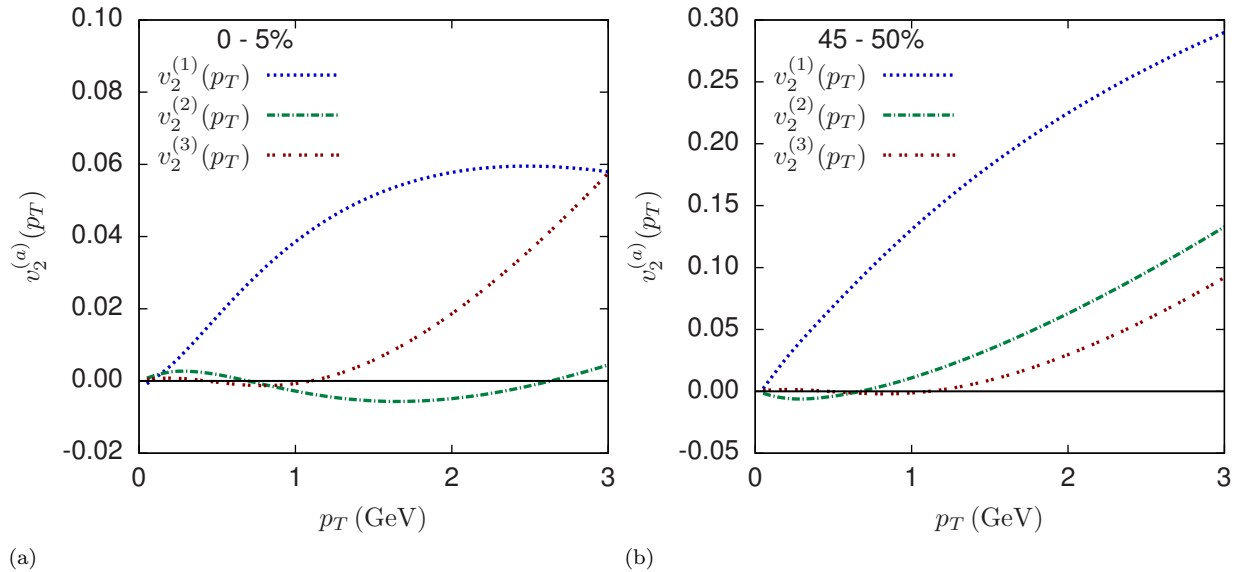


FIG. 4. The p_T dependence of the principal components of elliptic flow normalized by the average multiplicity, $v_2^{(a)}(p_T) \equiv V_2^{(a)}(p_T)/\langle dN/dp_T \rangle$, for central (0–5%) and peripheral collisions (45–50%).

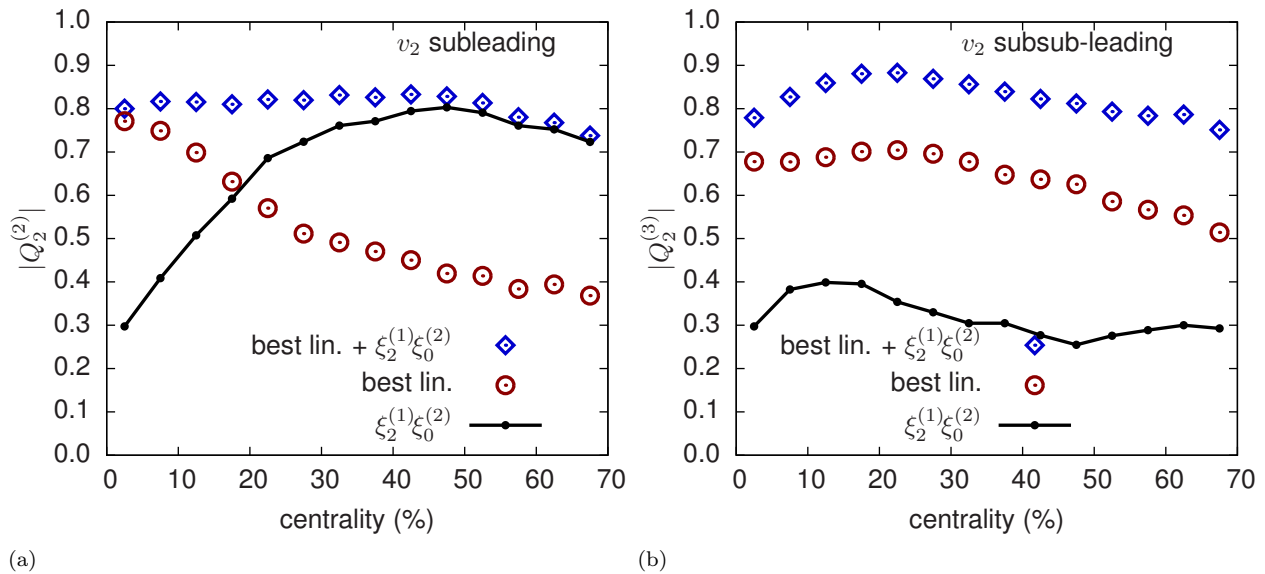


FIG. 5. Pearson correlation coefficient between the subleading elliptic flows and the best linear predictor [Eq. (11)] with and without the nonlinear mixing between the radial and leading elliptic flows, $\xi_2^{(1)}\xi_0^{(2)}$. (a) and (b) show the correlation coefficient for v_2 subleading and v_2 subsub-leading flows respectively.

2. Dependence on viscosity

Before leaving this section we will briefly comment on the viscosity dependence of these results. Figure 6 shows a typical result for a slightly larger shear viscosity, $\eta/s = 0.16$. As discussed above, the subleading elliptic flow [i.e., the event-by-event fluctuations in $V_2(p_T)$] is a result of the linear response to the first radial excitation of the elliptic eccentricity, and a nonlinear mix-

ing of radial flow fluctuations and the leading elliptic flow. In Fig. 6 we see that a slightly larger shear viscosity tends to preferentially damp the linear response leaving a stronger nonlinear signal. This is because the initial geometry driving the linear response has a significantly larger gradients due to the combined azimuthal and radial variations. Thus in Fig. 6 the linear response dominates the subleading flow only in very central collisions. These trends with centrality are qualitatively familiar from previous analyses of the effect of shear vis-

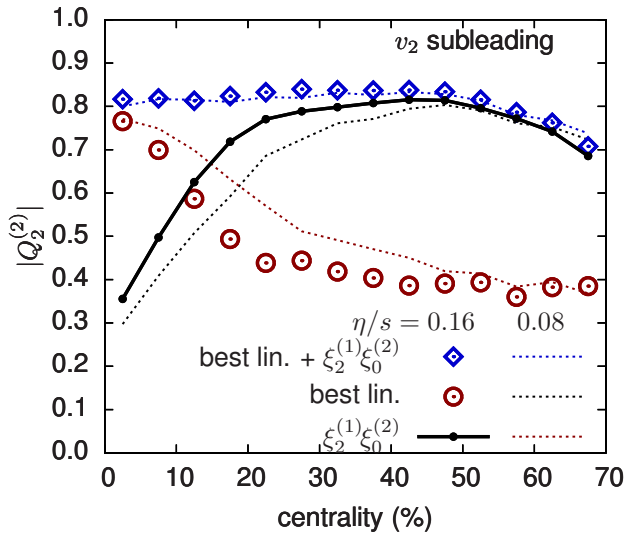


FIG. 6. Pearson correlation coefficients for the subleading elliptic flow at viscosity over entropy ratio $\eta/s = 0.16$. Dashed lines repeat $\eta/s = 0.08$ results from Fig. 5(a) for the ease of comparison.

cosity on the nonlinear mixing of harmonics [21, 25].

C. Triangular and directed flows

Triangular flow was extensively studied in our previous work [10]. For the sake of completeness we relegate several comparative plots to the Appendix. Previously, we constructed an optimal linear predictor $\varepsilon_3\{\rho(r)\}$ for the subleading triangular mode which characterizes the radially excited triangular geometry. As shown in Fig. 7(b), adding the nonlinear mixing term $\xi_0^{(2)}\xi_3^{(1)}$ to the best linear predictor marginally improves the already good correlation with the subleading flow in peripheral collisions.

Directed flow exhibits many similarities to triangular flow. Specifically the subleading directed flow is reasonably well correlated with the optimal linear predictor, characterizing the radially excited dipolar geometry. Nonlinear mixing between the leading directed flow and the radial flow is unimportant [see Fig. 7(a)].

D. The $n = 4$ and $n = 5$ harmonic flows

It is well known that the leading components of the $n = 4$ and $n = 5$ harmonics are determined by the nonlinear mixing of lower order harmonics in peripheral collisions [5, 18–21].

For comparison with other works [20, 26], in the Appendix in Figs. 13(d) and 14(d) we construct a predictor based on a linear combination of the eccentricities

$$\varepsilon_{4,4} + c_1\varepsilon_{2,2}\varepsilon_{2,2} \quad \text{for } n = 4, \quad (18)$$

$$\varepsilon_{5,5} + c_1\varepsilon_{2,2}\varepsilon_{3,3} \quad \text{for } n = 5, \quad (19)$$

where here and below the coefficient c_1 is adjusted to maximize the correlation with the flow. This predictor is compared to a linear combination of the optimal eccentricity $\varepsilon_n\{\rho(r)\}$ and the corresponding nonlinear mixings of the leading principal components

$$\varepsilon_4\{\rho(r)\} + c_1\xi_2^{(1)}\xi_2^{(1)} \quad \text{for } n = 4, \quad (20a)$$

$$\varepsilon_5\{\rho(r)\} + c_1\xi_2^{(1)}\xi_3^{(1)} \quad \text{for } n = 5. \quad (20b)$$

Both sets of predictors perform reasonably well, though the second set has a somewhat stronger correlation with the flow.

Returning to the subleading components, we first correlated with the best linear predictors, $\varepsilon_4\{\rho(r)\}$ and $\varepsilon_5\{\rho(r)\}$, with the corresponding subleading flow signals. As seen in Fig. 8 (the red circles), the correlation decreases rapidly with centrality, especially for v_4 . Motivated by Eq. (20) which predicts the event-by-event leading v_4 and v_5 in terms of v_2 and v_3 , we construct a predictor for the subleading v_4 and v_5 in terms of the fluctuations of v_2 and v_3 (see Secs. IIIB1 and IIIC, respectively). The full predictor reads

$$\varepsilon_4\{\rho(r)\} + c_1\xi_2^{(1)}\xi_2^{(2)}, \quad \text{for } n = 4, \quad (21a)$$

$$\varepsilon_5\{\rho(r)\} + c_1\xi_2^{(1)}\xi_3^{(2)} + c_2\xi_3^{(1)}\xi_2^{(2)}, \quad \text{for } n = 5. \quad (21b)$$

Including the mixings between the subleading v_2 and v_3 and the corresponding leading components greatly improves the correlation in mid-central bins (the blue diamonds). Finally, in an effort to improve the v_4 predictor in the most peripheral bins we have added additional nonlinear mixings between the radial flow and the leading principal components

$$\varepsilon_4\{\rho(r)\} + c_1\xi_2^{(1)}\xi_2^{(2)} + c_2\xi_4^{(1)}\xi_0^{(2)}, \quad \text{for } n = 4, \quad (22a)$$

$$\varepsilon_5\{\rho(r)\} + c_1\xi_2^{(1)}\xi_3^{(2)} + c_2\xi_3^{(1)}\xi_2^{(2)} + c_3\xi_5^{(1)}\xi_0^{(2)}, \quad \text{for } n = 5. \quad (22b)$$

As seen in Fig. 8(a) (the grey line) the coupling to the radial flow improves the correlation between the subleading v_4 and the predictor in peripheral collisions. On the other hand, for v_5 , Fig. 8(b), all of the information about the coupling to the radial flow is already included in Eq. (21b) and adding v_0 does not improve the correlation.

IV. DISCUSSION

In this paper we classified the event-by-event fluctuations of the momentum dependent Fourier harmonics $V_n(p_T)$ for $n = 0-5$ by performing a principal component analysis of the two-particle correlation matrix in hydrodynamic simulations of heavy ion collisions. The leading principal component for each harmonic is very strongly correlated with the integrated flow, and therefore this

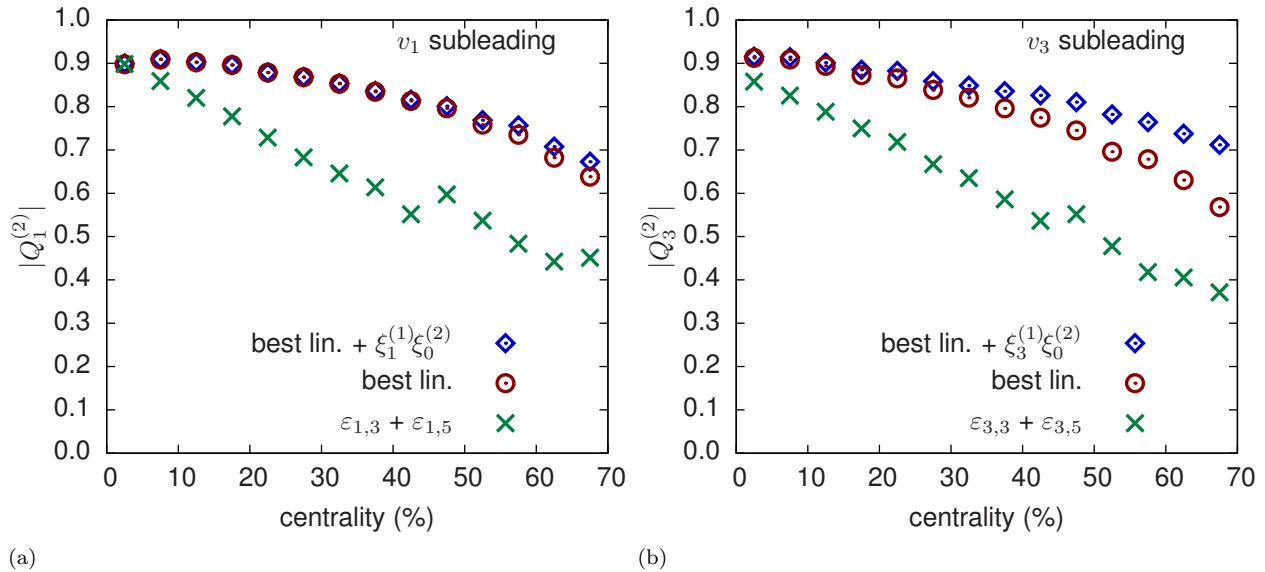


FIG. 7. Pearson correlation coefficient between the subleading (a) directed and (b) triangular flows and the best linear predictor with and without radial flow mixing.

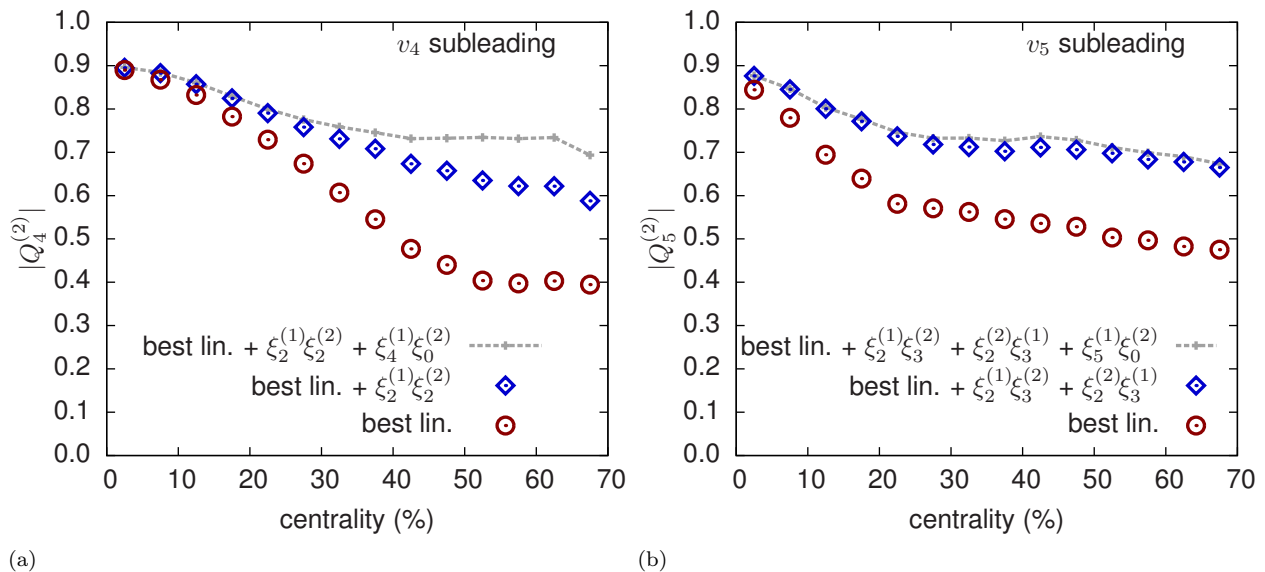


FIG. 8. Pearson correlation coefficient between the subleading v_4 and v_5 flows and the best linear predictor with and without several nonlinear terms [see Eqs. (21) and (22)].

component is essentially the familiar $v_n(p_T)$ measured in the event plane. The *subleading* components describe additional p_T dependent fluctuations of the magnitude and phase of $v_n(p_T)$. This paper focuses on the physical origins of the subleading flows, which are the largest source of factorization breaking in hydrodynamics.

Our systematic study started by placing radial flow (the $n = 0$ harmonic) in the same framework as the other harmonic flows. We identified the subleading $n = 0$ principal component with mean p_T fluctuations and confirmed (as is well known [23, 24]) that these fluctuations

are predicted by the variance of the radial size of the fireball.

The subleading directed and triangular flows were shown to be a linear response to the radial excitations of the corresponding eccentricity of the initial geometry. In these cases a generalized eccentricity $\varepsilon_n\{\rho(r)\}$ with an optimized radial weight (describing the radial excitation) provides a good predictor for the subleading flows (Fig. 7). This extends our previous analysis of v_3 to v_1 [10].

Next, we investigated the nature of the subleading el-

liptic flows. The principal component analysis reveals that in central collisions there are two comparable sources of subleading elliptic flow, but they have strikingly different centrality dependence (see Figs. 3 and 4). In mid-peripheral collisions the first subleading component mainly reflects a nonlinear mixing between elliptic and radial flows, and this component is only weakly correlated with the radially excitations of the elliptic geometry. The second subleading component in this centrality range is substantially smaller and more closely reflects the radial excitations. In more central collisions, however, the nonlinear mixing with the average elliptic flow becomes small, and the sub and subsub-leading principal components become comparable in size. Thus, the rapid centrality dependence of factorization breaking in v_2 is the result of an interplay between the linear response to the fluctuating elliptic geometry, and the nonlinear mixing of the radial and average elliptic flows.

This nonlinear mixing can be confirmed experimentally by measuring the correlations between the principal components $\langle \xi_2^{(2)} (\xi_2^{(1)} \xi_0^{(2)})^* \rangle$ which is predicted in Fig. 5. The prediction is that three point correlation between the subleading elliptic event plane, the mean p_T fluctuations, and the leading elliptic event plane defined by the Q_2 vector, i.e.,

$$\frac{\langle \xi_2^{(2)} \delta p_T Q_2^* \rangle}{\sqrt{\langle (\delta p_T)^2 \rangle \langle |Q_2|^2 \rangle}}, \quad (23)$$

changes rapidly from central to midperipheral collisions. This correlation is analogous to the three plane correlations such as $\langle V_5 (V_2 V_3)^* \rangle$ measured previously [5].

Finally, we studied factorization breaking in v_4 and v_5 . With the comprehensive understanding of the fluctuations of v_2 and v_3 described above, the corresponding fluctuations in v_4 and v_5 were naturally explained as the nonlinear mixing of subleading v_2 and v_3 with their leading counterparts, together with linear response to the quadrangular and pentagonal geometries (see Fig. 8).

The study of the fluctuations in the harmonics spectrum presented here shows the power of the principal component method in elucidating the physics which drive the event-by-event flow. We hope that this motivates a comprehensive experimental program measuring the principal components and their correlations for $n = 0 - 5$. Such an analysis would clarify the initial state in typical and ultra-central events with unprecedented precision, and would strongly constrain the dynamical response of the quark gluon plasma.

ACKNOWLEDGMENTS

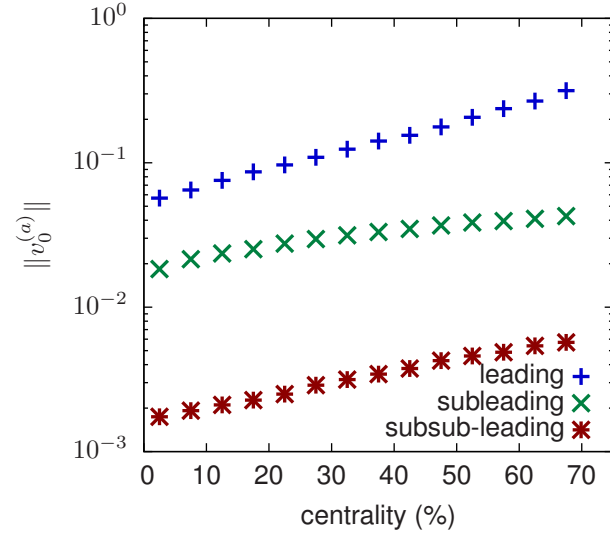
We thank Jean-Yves Ollitrault, Wei Li, and Jiangyong Jia for continued interest. We especially thank Soumya Mohapatra for simulating hydro events. This work was supported by the U.S. Department of Energy under Contract No. DE-FG-88ER40388

-
- [1] Ulrich Heinz and Raimond Snellings, “Collective flow and viscosity in relativistic heavy-ion collisions,” *Ann. Rev. Nucl. Part. Sci.* **63**, 123–151 (2013).
 - [2] Matthew Luzum and Hannah Petersen, “Initial State Fluctuations and Final State Correlations in Relativistic Heavy-Ion Collisions,” *J. Phys.* **G41**, 063102 (2014), [arXiv:1312.5503 \[nucl-th\]](#).
 - [3] Vardan Khachatryan *et al.* (CMS), “Evidence for transverse momentum and pseudorapidity dependent event plane fluctuations in PbPb and pPb collisions,” *Phys. Rev.* **C92**, 034911 (2015), [arXiv:1503.01692 \[nucl-ex\]](#).
 - [4] Georges Aad *et al.* (ATLAS), “Measurement of event-plane correlations in $\sqrt{s_{NN}} = 2.76$ TeV lead-lead collisions with the ATLAS detector,” *Phys. Rev.* **C90**, 024905 (2014), [arXiv:1403.0489 \[hep-ex\]](#).
 - [5] Georges Aad *et al.* (ATLAS), “Measurement of the correlation between flow harmonics of different order in lead-lead collisions at $\sqrt{s_{NN}} = 2.76$ TeV with the ATLAS detector,” *Phys. Rev.* **C92**, 034903 (2015), [arXiv:1504.01289 \[hep-ex\]](#).
 - [6] Jaroslav Adam *et al.* (ALICE), “Event shape engineering for inclusive spectra and elliptic flow in Pb-Pb collisions at $\sqrt{s_{NN}} = 2.76$ TeV,” [arXiv:1507.06194 \[nucl-ex\]](#).
 - [7] L. Adamczyk *et al.* (STAR), “Long-range pseudorapidity dihadron correlations in d +Au collisions at $\sqrt{s_{NN}} = 200$ GeV,” *Phys. Lett.* **B747**, 265–271 (2015), [arXiv:1502.07652 \[nucl-ex\]](#).
 - [8] A. Adare *et al.* (PHENIX), “Measurements of elliptic and triangular flow in high-multiplicity $^3\text{He}+\text{Au}$ collisions at $\sqrt{s_{NN}} = 200$ GeV,” *Phys. Rev. Lett.* **115**, 142301 (2015), [arXiv:1507.06273 \[nucl-ex\]](#).
 - [9] Rajeev S. Bhalerao, Jean-Yves Ollitrault, Subrata Pal, and Derek Teaney, “Principal component analysis of event-by-event fluctuations,” *Phys. Rev. Lett.* **114**, 152301 (2015), [arXiv:1410.7739 \[nucl-th\]](#).
 - [10] Aleksas Mazeliauskas and Derek Teaney, “Subleading harmonic flows in hydrodynamic simulations of heavy ion collisions,” *Phys. Rev.* **C91**, 044902 (2015), [arXiv:1501.03138 \[nucl-th\]](#).
 - [11] Fernando G. Gardim, Frederique Grassi, Matthew Luzum, and Jean-Yves Ollitrault, “Breaking of factorization of two-particle correlations in hydrodynamics,” *Phys. Rev.* **C87**, 031901 (2013), [arXiv:1211.0989 \[nucl-th\]](#).
 - [12] K. Aamodt *et al.* (ALICE), “Harmonic decomposition of two-particle angular correlations in Pb-Pb collisions at $\sqrt{s_{NN}} = 2.76$ TeV,” *Phys. Lett.* **B708**, 249–264 (2012), [arXiv:1109.2501 \[nucl-ex\]](#).
 - [13] Georges Aad *et al.* (ATLAS), “Measurement of the azimuthal anisotropy for charged particle production in $\sqrt{s_{NN}} = 2.76$ TeV lead-lead collisions with the ATLAS detector,” *Phys. Rev.* **C86**, 014907 (2012), [arXiv:1203.3087 \[hep-ex\]](#).
 - [14] Georges Aad *et al.* (ATLAS), “Measurement of long-

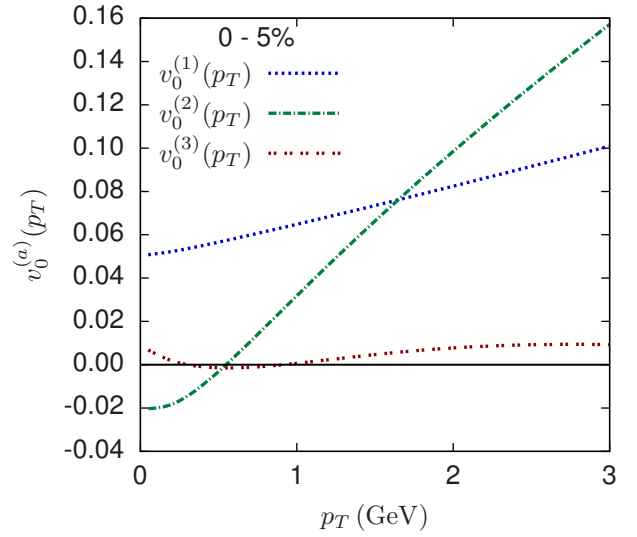
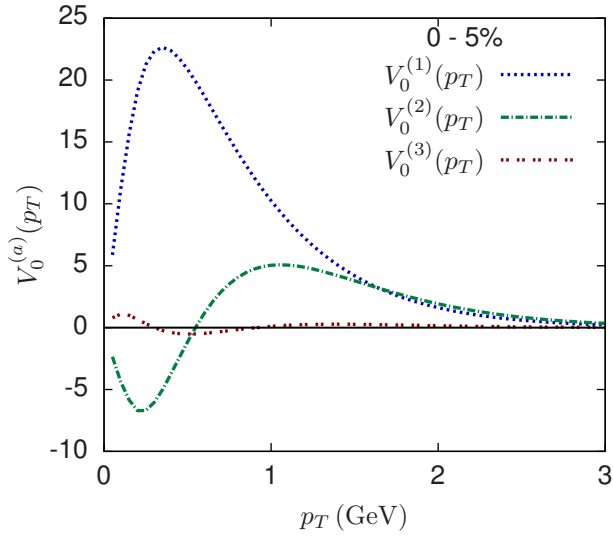
- range pseudorapidity correlations and azimuthal harmonics in $\sqrt{s_{NN}} = 5.02$ TeV proton-lead collisions with the ATLAS detector,” *Phys. Rev.* **C90**, 044906 (2014), [arXiv:1409.1792 \[hep-ex\]](#).
- [15] Ulrich Heinz, Zhi Qiu, and Chun Shen, “Fluctuating flow angles and anisotropic flow measurements,” *Phys. Rev.* **C87**, 034913 (2013), [arXiv:1302.3535 \[nucl-th\]](#).
- [16] Igor Kozlov, Matthew Luzum, Gabriel Denicol, Sangyong Jeon, and Charles Gale, “Transverse momentum structure of pair correlations as a signature of collective behavior in small collision systems,” [arXiv:1405.3976 \[nucl-th\]](#).
- [17] B. Alver, M. Baker, C. Loizides, and P. Steinberg, “The PHOBOS Glauber Monte Carlo,” [arXiv:0805.4411 \[nucl-ex\]](#).
- [18] Nicolas Borghini and Jean-Yves Ollitrault, “Momentum spectra, anisotropic flow, and ideal fluids,” *Phys. Lett.* **B642**, 227–231 (2006), [arXiv:nucl-th/0506045 \[nucl-th\]](#).
- [19] Zhi Qiu and Ulrich W. Heinz, “Event-by-event shape and flow fluctuations of relativistic heavy-ion collision fireballs,” *Phys. Rev.* **C84**, 024911 (2011), [arXiv:1104.0650 \[nucl-th\]](#).
- [20] Fernando G. Gardim, Frederique Grassi, Matthew Luzum, and Jean-Yves Ollitrault, “Mapping the hydrodynamic response to the initial geometry in heavy-ion collisions,” *Phys. Rev.* **C85**, 024908 (2012), [arXiv:1111.6538 \[nucl-th\]](#).
- [21] Derek Teaney and Li Yan, “Non linearities in the harmonic spectrum of heavy ion collisions with ideal and viscous hydrodynamics,” *Phys. Rev.* **C86**, 044908 (2012), [arXiv:1206.1905 \[nucl-th\]](#).
- [22] Mikko Laine and York Schroder, “Quark mass thresholds in QCD thermodynamics,” *Phys. Rev.* **D73**, 085009 (2006), [arXiv:hep-ph/0603048 \[hep-ph\]](#).
- [23] Wojciech Broniowski, Mikolaj Chojnacki, and Lukasz Obara, “Size fluctuations of the initial source and the event-by-event transverse momentum fluctuations in relativistic heavy-ion collisions,” *Phys. Rev.* **C80**, 051902 (2009), [arXiv:0907.3216 \[nucl-th\]](#).
- [24] Piotr Bozek and Wojciech Broniowski, “Transverse-momentum fluctuations in relativistic heavy-ion collisions from event-by-event viscous hydrodynamics,” *Phys. Rev.* **C85**, 044910 (2012), [arXiv:1203.1810 \[nucl-th\]](#).
- [25] Zhi Qiu and Ulrich Heinz, “Hydrodynamic event-plane correlations in Pb+Pb collisions at $\sqrt{s} = 2.76$ ATeV,” *Phys. Lett.* **B717**, 261–265 (2012), [arXiv:1208.1200 \[nucl-th\]](#).
- [26] Fernando G. Gardim, Jacquelyn Noronha-Hostler, Matthew Luzum, and Frdrique Grassi, “Effects of viscosity on the mapping of initial to final state in heavy ion collisions,” *Phys. Rev.* **C91**, 034902 (2015), [arXiv:1411.2574 \[nucl-th\]](#).

APPENDIX: LIST OF FIGURES

Here we present a comprehensive catalog of plots for each harmonic $n = 0-5$. Centrality dependence of flow magnitudes for $n = 0$, appearing as Fig. 3 in the text above, is repeated here as Fig. 9(a), and analogous plots for other harmonics are given in Figs. 10-14(a). The p_T dependence of normalized principal components for radial and elliptic flows in central (0-5%) collisions shown in Figs. 2(a) and 4(a) are reproduced as Figs. 9(c) and 11(c) and complemented with Figs. 10(c) and 12-14(c). Additionally, Figs. 9-14(b) depict the same principal components, but without normalization by average multiplicity $\langle dN/dp_T \rangle$. Finally, in the paper we showed the Pearson correlation coefficients for the subleading flows for each harmonic $n = 0-5$ in Figs. 2(b), 5(a), 7(a), 7(b), 8(a) and 8(b), while in this appendix we show results for both leading and subleading flows in the series of figures Figs. 9-14(d) and Figs. 9-14(e).

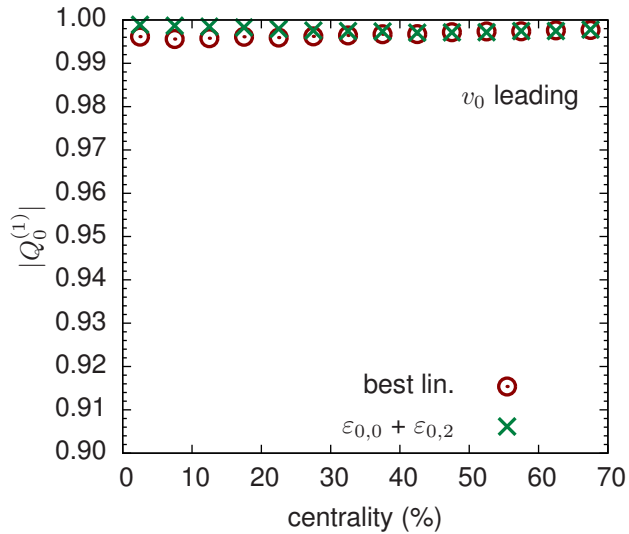


(a) Centrality dependence of the (scaled) magnitudes of flows $\|v_0^{(a)}\|$.

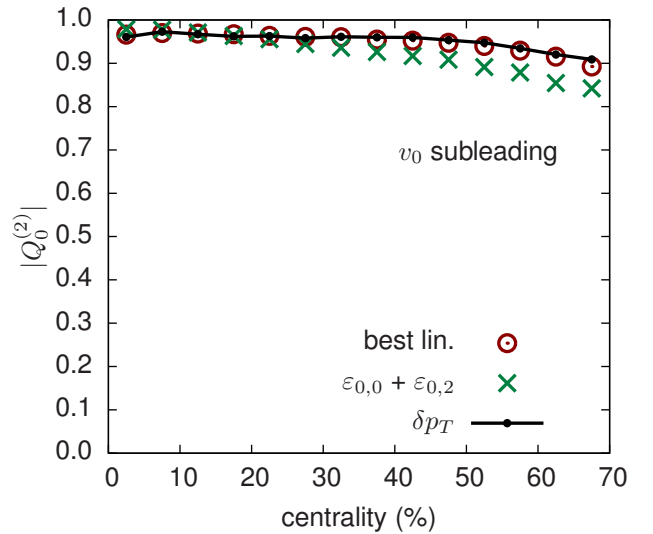


(b) Momentum dependence of principal flow vectors $V_0^{(a)}(p_T)$ in central collisions.

(c) Principal flow vectors divided by the average multiplicity, $v_0^{(a)}(p_T) \equiv V_0^{(a)}(p_T) / \langle dN/dp_T \rangle$.

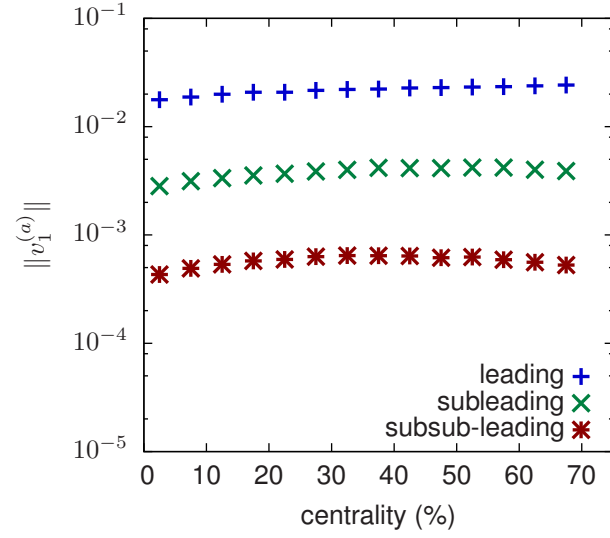


(d) Pearson correlation coefficient between the leading flow (zero suppressed for clarity) and several predictors.

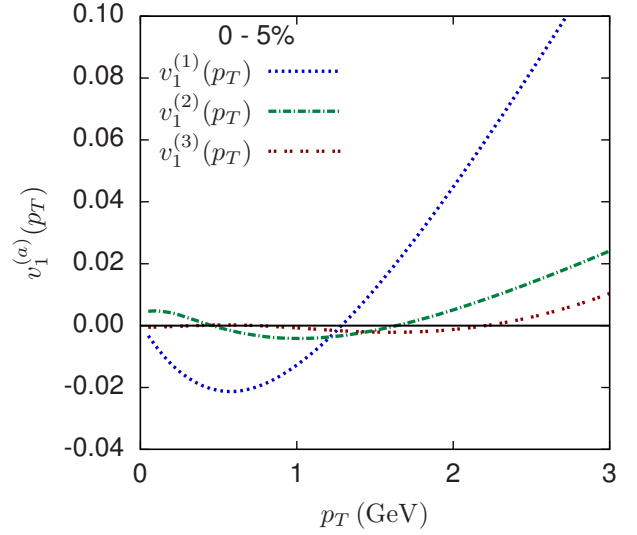
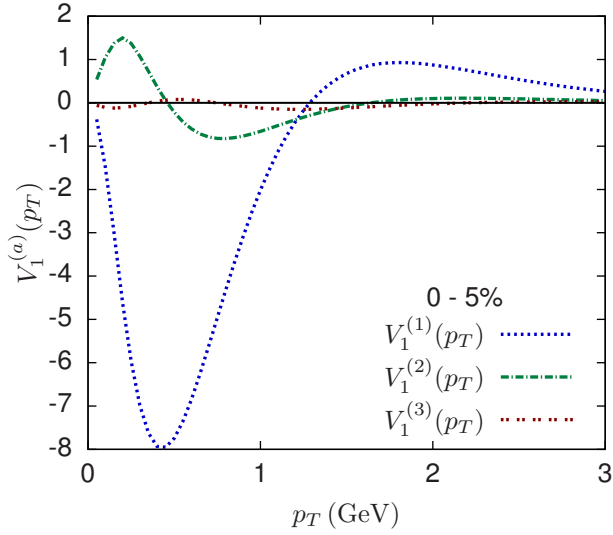


(e) Pearson correlation coefficient between the subleading flow and several predictors.

FIG. 9. $n = 0$

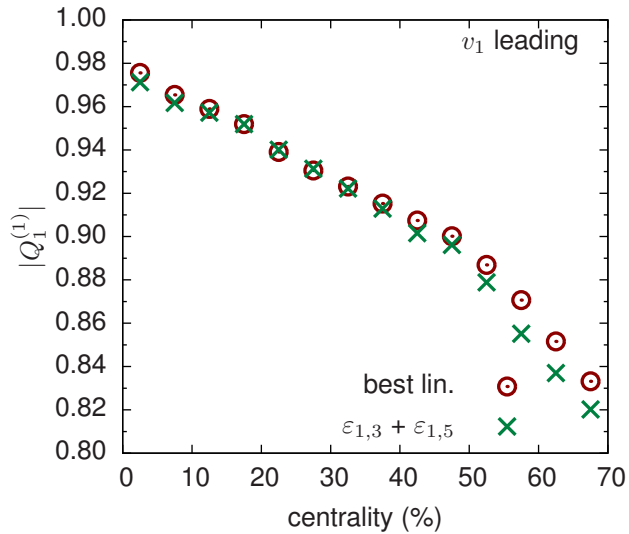


(a) Centrality dependence of the (scaled) magnitudes of flows $\|v_1^{(a)}\|$.

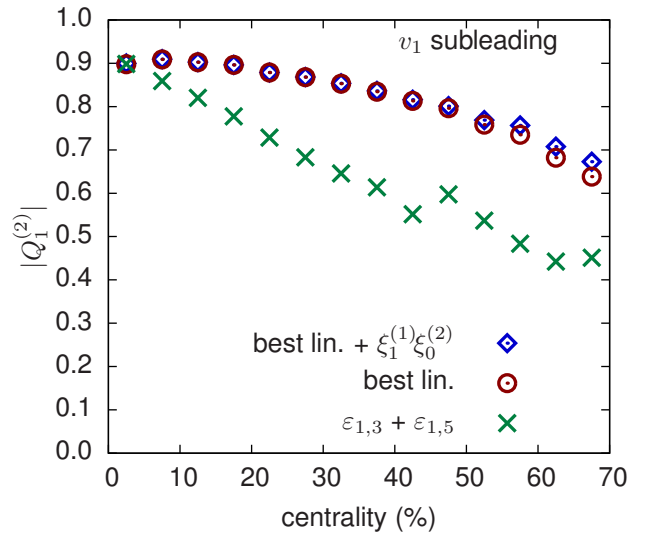


(b) Momentum dependence of principal flow vectors $V_1^{(a)}(p_T)$ in central collisions.

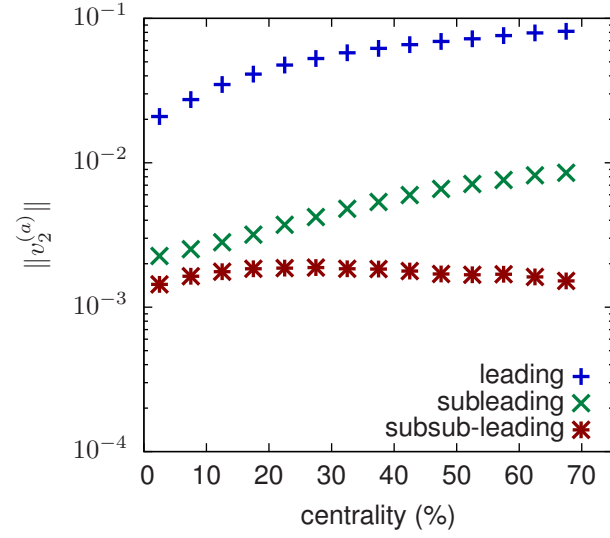
(c) Principal flow vectors divided by the average multiplicity, $v_1^{(a)}(p_T) \equiv V_1^{(a)}(p_T) / \langle dN/dp_T \rangle$.



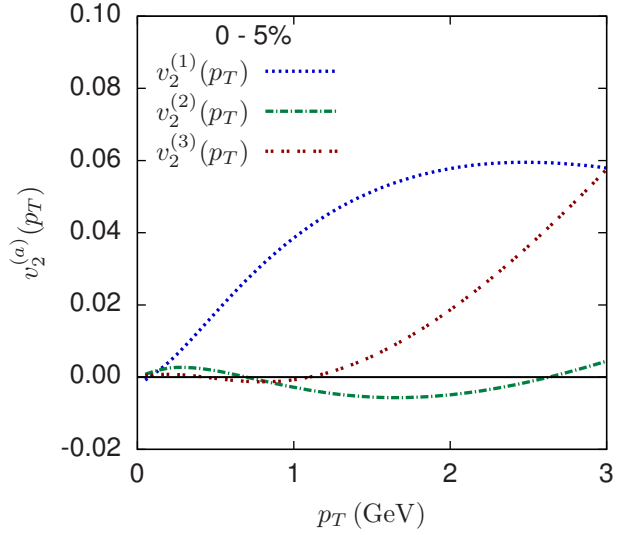
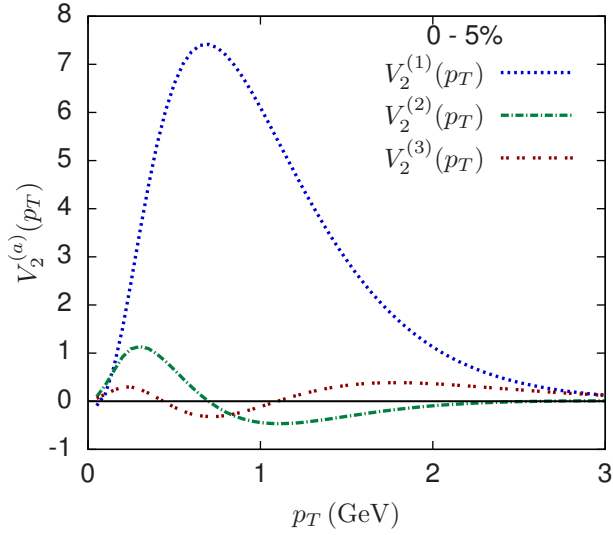
(d) Pearson correlation coefficient between the leading flow (zero suppressed for clarity) and several predictors.



(e) Pearson correlation coefficient between the subleading flow and several predictors.

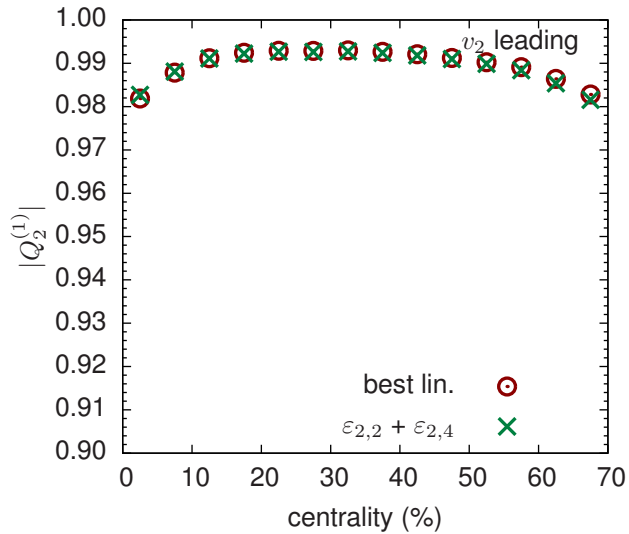


(a) Centrality dependence of the (scaled) magnitudes of flows $\|v_2^{(a)}\|$.

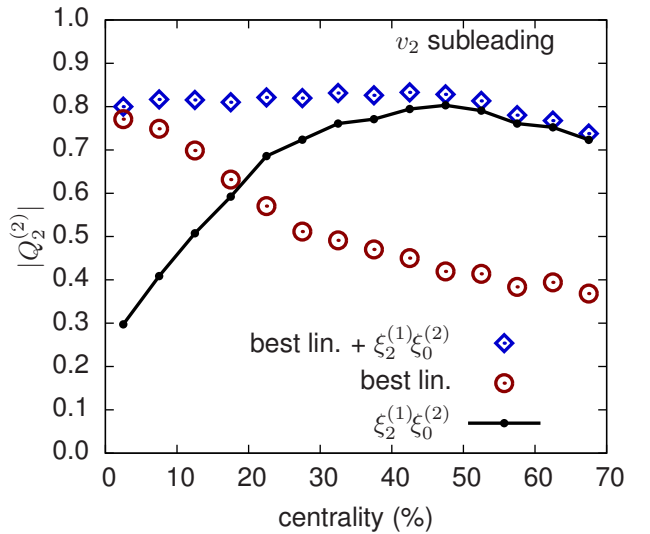


(b) Momentum dependence of principal flow vectors $V_2^{(a)}(p_T)$ in central collisions.

(c) Principal flow vectors divided by the average multiplicity, $v_2^{(a)}(p_T) \equiv V_2^{(a)}(p_T) / \langle dN/dp_T \rangle$.

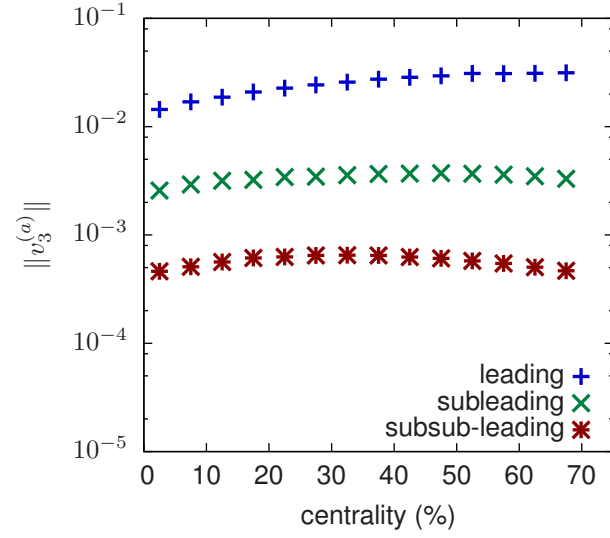


(d) Pearson correlation coefficient between the leading flow (zero suppressed for clarity) and several predictors.

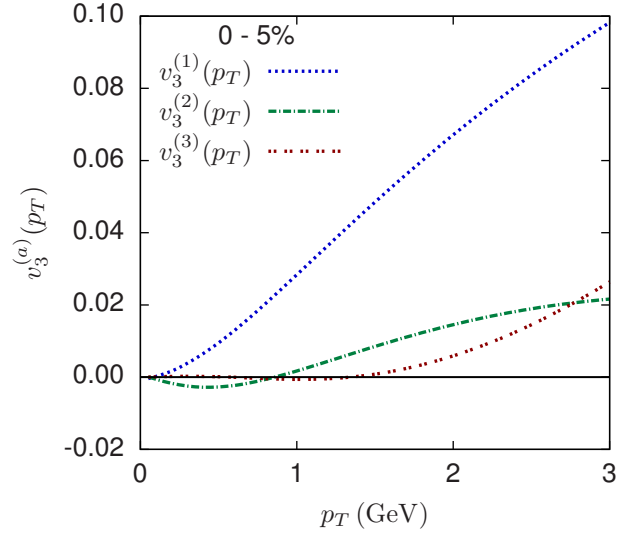
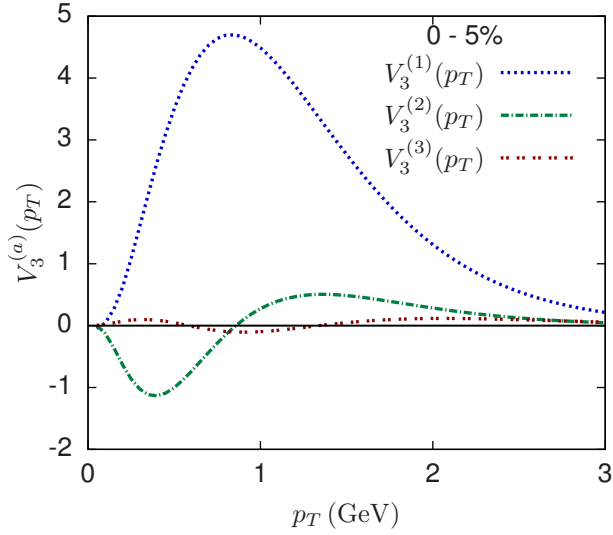


(e) Pearson correlation coefficient between the subleading flow and several predictors.

FIG. 11. $n = 2$

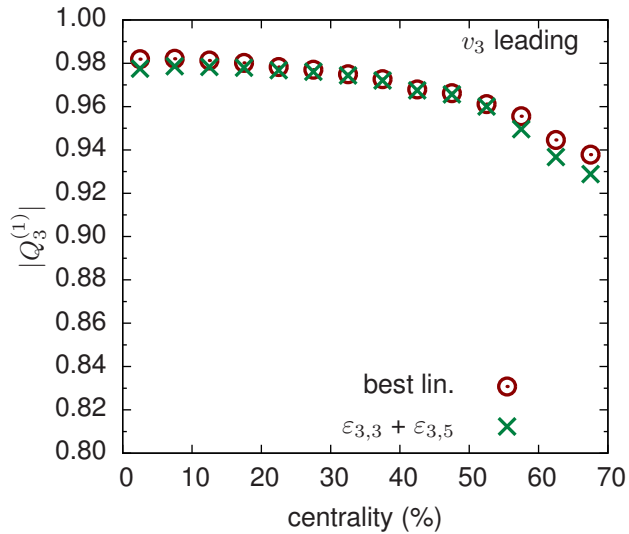


(a) Centrality dependence of the (scaled) magnitudes of flows $\|v_3^{(a)}\|$.

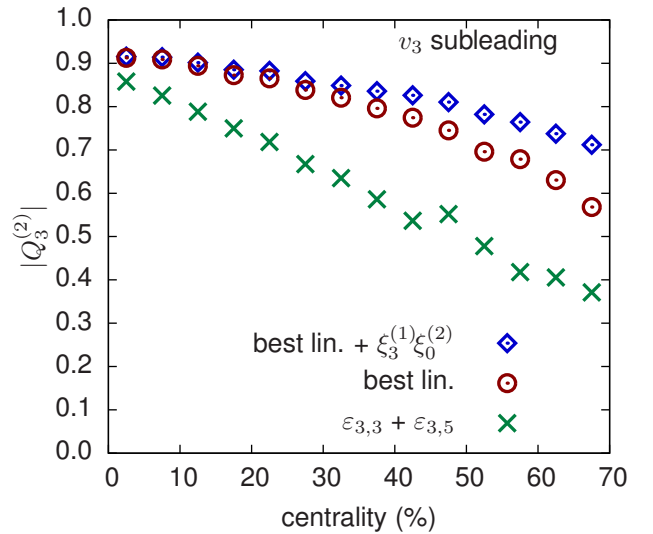


(b) Momentum dependence of principal flow vectors $V_3^{(a)}(p_T)$ in central collisions.

(c) Principal flow vectors divided by the average multiplicity, $v_3^{(a)}(p_T) \equiv V_3^{(a)}(p_T) / \langle dN/dp_T \rangle$.

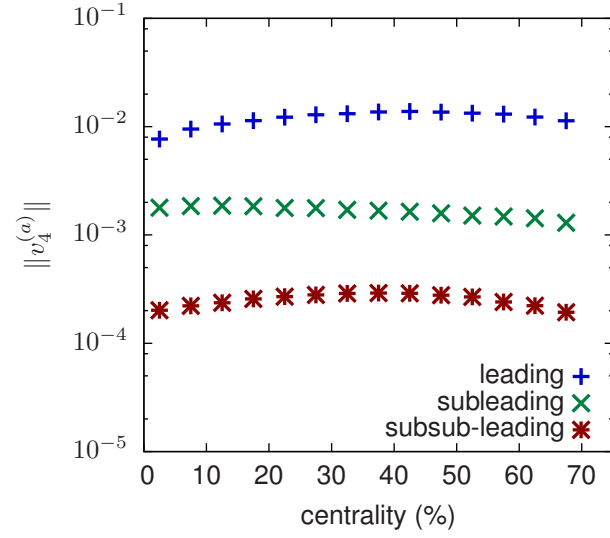


(d) Pearson correlation coefficient between the leading flow (zero suppressed for clarity) and several predictors.

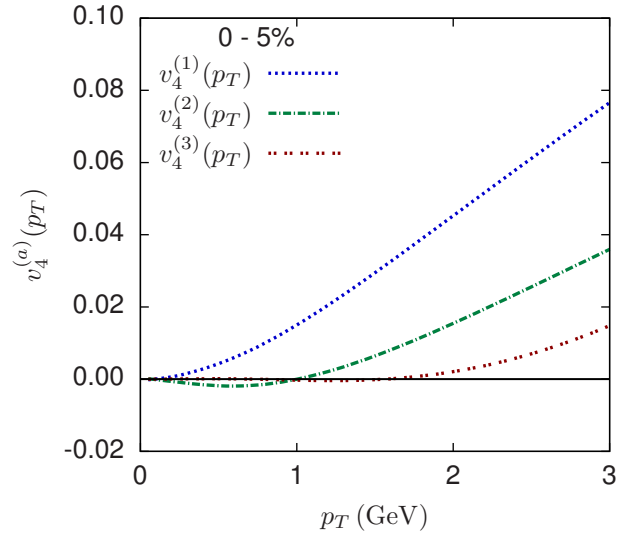
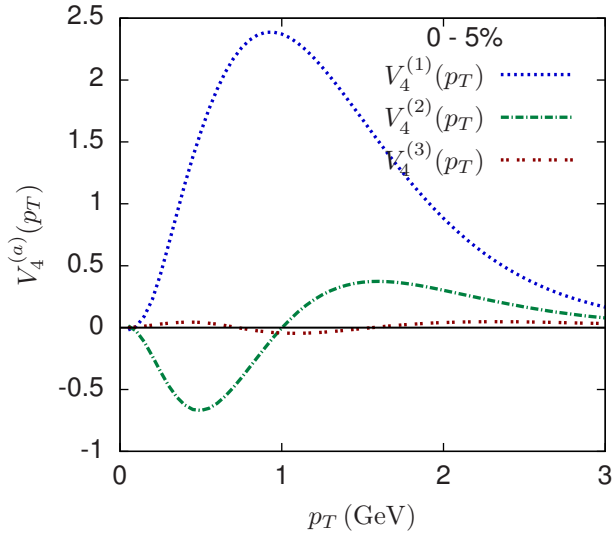


(e) Pearson correlation coefficient between the subleading flow and several predictors.

FIG. 12. $n = 3$

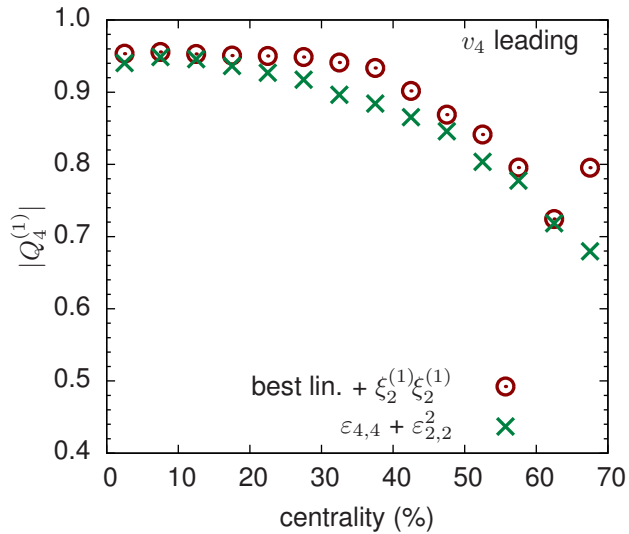


(a) Centrality dependence of the (scaled) magnitudes of flows $\|v_4^{(a)}\|$.

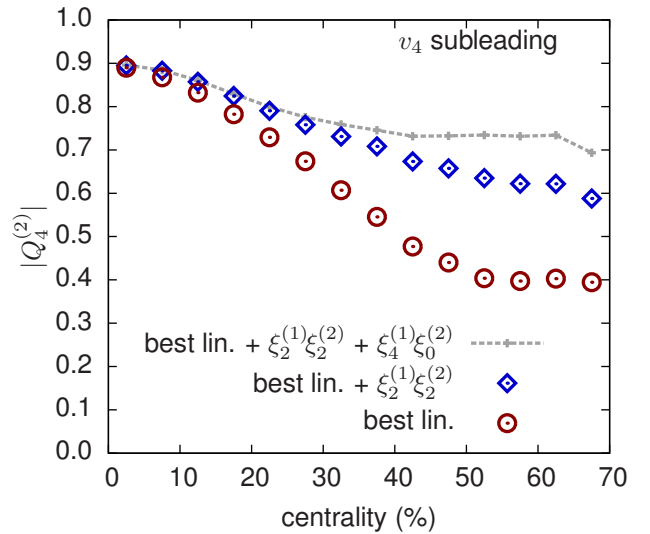


(b) Momentum dependence of principal flow vectors $V_4^{(a)}(p_T)$ in central collisions.

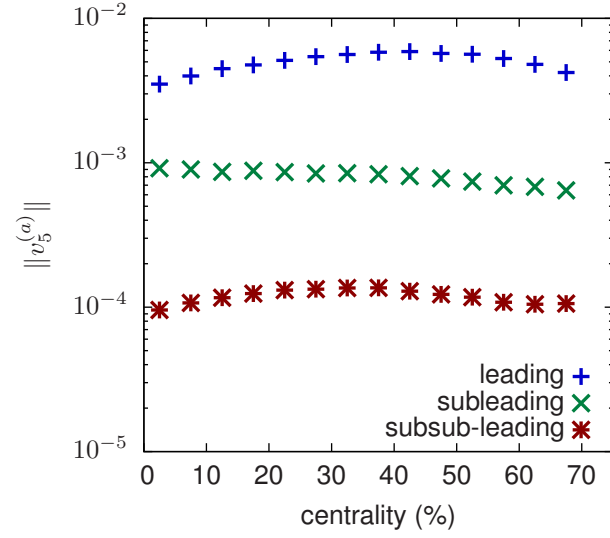
(c) Principal flow vectors divided by the average multiplicity, $v_4^{(a)}(p_T) \equiv V_4^{(a)}(p_T) / \langle dN/dp_T \rangle$.



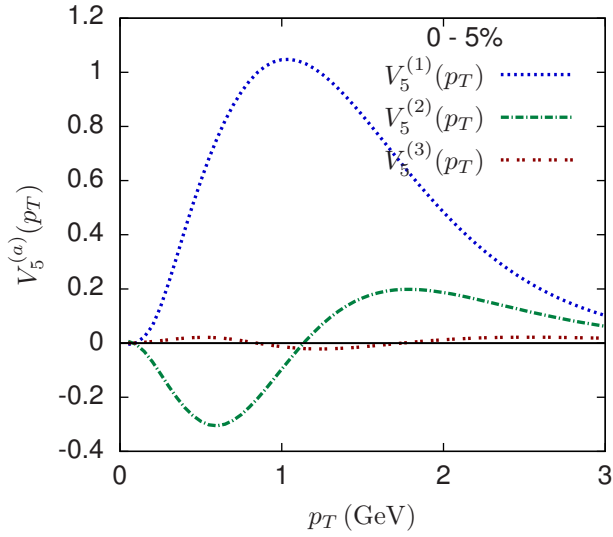
(d) Pearson correlation coefficient between the leading flow (zero suppressed for clarity) and several predictors.



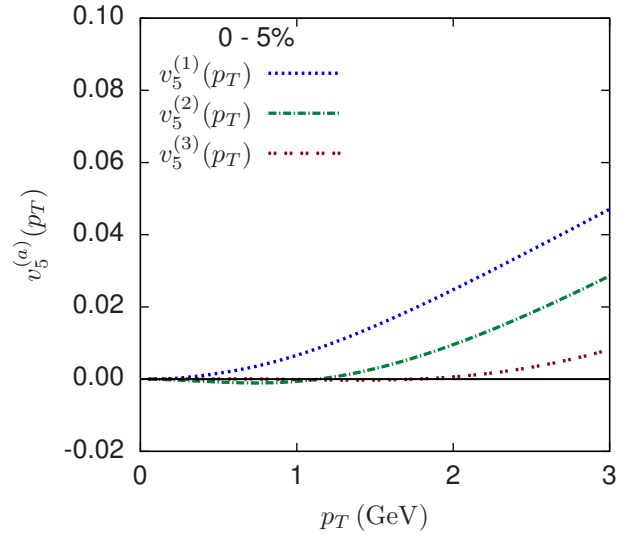
(e) Pearson correlation coefficient between the subleading flow and several predictors.



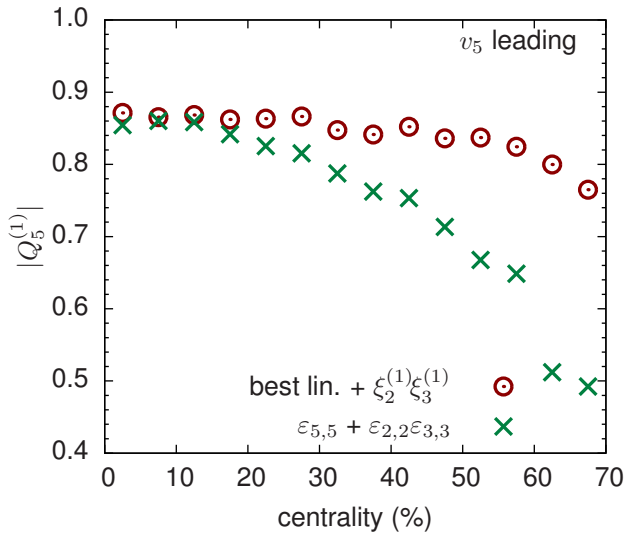
(a) Centrality dependence of the (scaled) magnitudes of flows $\|v_5^{(a)}\|$.



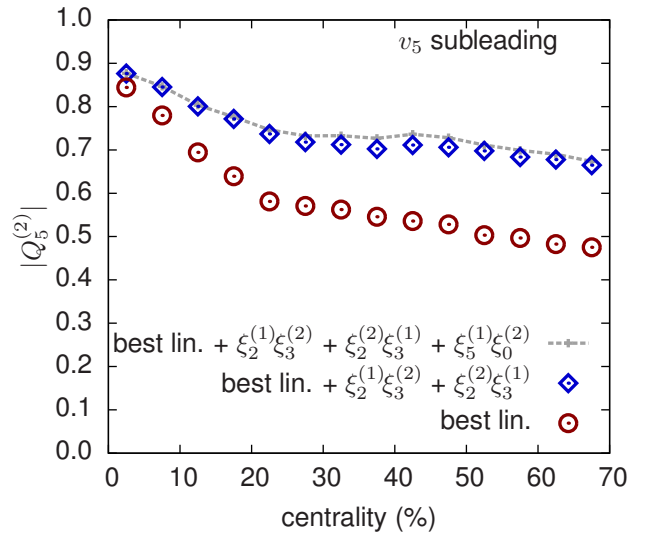
(b) Momentum dependence of principal flow vectors $V_5^{(a)}(p_T)$ in central collisions.



(c) Principal flow vectors divided by the average multiplicity, $v_5^{(a)}(p_T) \equiv V_5^{(a)}(p_T) / \langle dN/dp_T \rangle$.



(d) Pearson correlation coefficient between the leading flow (zero suppressed for clarity) and several predictors.



(e) Pearson correlation coefficient between the subleading flow and several predictors.

FIG. 14. $n = 5$